



# Monodispersed $\text{CuFe}_2\text{O}_4$ nanoparticles anchored on natural kaolinite as highly efficient peroxymonosulfate catalyst for bisphenol A degradation

Xiongbo Dong<sup>a,b</sup>, Bangxing Ren<sup>b</sup>, Zhiming Sun<sup>a,\*</sup>, Chunquan Li<sup>a</sup>, Xiangwei Zhang<sup>a</sup>, Minghao Kong<sup>b</sup>, Shuilin Zheng<sup>a,\*</sup>, Dionysios D. Dionysiou<sup>b,\*</sup>

<sup>a</sup> School of Chemical and Environmental Engineering, China University of Mining and Technology (Beijing), Beijing, 100083, PR China

<sup>b</sup> Environmental Engineering and Science Program, Department of Chemical and Environmental Engineering (ChEE), University of Cincinnati, Cincinnati, OH, 45221, USA

## ARTICLE INFO

### Keywords:

Copper ferrite  
Kaolinite  
Peroxymonosulfate  
Sulfate radical  
BPA

## ABSTRACT

In this study,  $\text{CuFe}_2\text{O}_4$ /kaolinite catalysts were fabricated through a facile citrate combustion method and were evaluated for their efficiency to activate peroxymonosulfate (PMS) towards the destruction of bisphenol A (BPA). The prepared catalysts were systematically characterized to explore the relationship between their characteristics and catalytic activities. In general, higher specific surface area, larger pore volume, more hydroxyl groups, and more accessible reactive sites of 40%- $\text{CuFe}_2\text{O}_4$ /kaolinite contributed to the greater catalytic activity in peroxymonosulfate activation for BPA degradation compared to bare  $\text{CuFe}_2\text{O}_4$ . Monodispersed  $\text{CuFe}_2\text{O}_4$  nanoparticles were uniformly anchored on the surface of kaolinite with Fe–O–Al bond, which prevented leaching of metal ions and contributed to the excellent reusability. The sulfate radicals produced in the  $\text{CuFe}_2\text{O}_4$ /kaolinite/PMS system were proved as the predominant radical species through electron spin resonance (ESR) and radical quenching experiments. Based on the results of X-ray photoelectron spectroscopy (XPS) and attenuated total reflectance – Fourier transform infrared spectra (ATR-FTIR), two main possible pathways of sulfate radicals generation were proposed: the generation and decomposition of  $\equiv\text{Cu(II)}\cdot(\text{HO})\text{OSO}_3^-$  ( $\text{Cu(II)}/\text{Cu(III)}$ ) and  $\text{Cu(III)}/\text{Cu(II)}$  redox reaction) and the oxidation of  $\equiv\text{Fe(II)}$ . Moreover, the BPA degradation pathway was proposed through the identification of transformation products. This work provides an interesting insight for PMS activation by the high-efficient natural mineral-based catalysts for wastewater reclamation.

## 1. Introduction

Bisphenol A (2,2-bis(4-hydroxyphenyl) propane, BPA), as one of the most important produced organic chemicals, is intensively used in the production of polycarbonate plastic and epoxy resins [1,2]. Unfortunately, near a quarter of consumed BPA is continuously released into the environment, with the potential to lead to endocrine disrupting effects in both aquatic wildlife and human beings through hindering or interfering functions of hormones [3,4]. To address this issue, various traditional treatment methods based on chemical, physical and biological techniques have been extensively investigated over the years for efficiently removing BPA from contaminated water [5–7]. Among these technologies, advanced oxidation processes (AOPs), such as Fenton [8], ozonation [9], and photocatalysis [10,11], have shown promising prospect for wastewater reclamation because of their environmental friendliness, convenient operation and efficient oxidation for BPA.

In recent years, sulfate radical  $\cdot\text{OH}$  and  $\text{SO}_4^{\cdot-}$  based advanced oxidation processes (AOPs) attracted increasing interest [12–15]

because of some promising results in the degradation of several recalcitrant organic contaminants in water. Among other factors, this was in part attributed to the relatively long lifetime (30–40  $\mu\text{s}$ ) and high redox potential (2.5–3.1 V) of  $\text{SO}_4^{\cdot-}$ . In general, peroxymonosulfate (PMS) or peroxydisulfate (PDS) can be used as peroxides to generate sulfate radical ( $\text{SO}_4^{\cdot-}$ ) by transition metal ions (Co, Fe, Cu, Mn, Ru, Ag, V, Ce, and Ni) or other oxidants [16–18], ultrasound [19], UV [20], heat [21], and electrochemical processes [22]. The use of transition metal oxidants to activate PMS or PDS is of particular interest because of their co-presence in some of the contaminated waters and their availability in various forms, including as solid catalysts and composites that can be reused. Nevertheless, the heavy metal ions generated during leaching of various solids catalysts during the PMS activation process could result in secondary waste pollution, which limits practical application of this process for wastewater reclamation.

Recently, crystalline  $\text{CuFe}_2\text{O}_4$  nanoparticles with spinel structure have received great attention for catalyzing PMS and presented high catalytic activity and low leaching of metal ions (Table S1). However,

\* Corresponding authors.

E-mail addresses: [zhimingsun@cumtb.edu.cn](mailto:zhimingsun@cumtb.edu.cn) (Z. Sun), [zhengsl@cumtb.edu.cn](mailto:zhengsl@cumtb.edu.cn) (S. Zheng), [dionysios.d.dionysiou@uc.edu](mailto:dionysios.d.dionysiou@uc.edu) (D.D. Dionysiou).

<https://doi.org/10.1016/j.apcatb.2019.04.052>

Received 25 January 2019; Received in revised form 14 April 2019; Accepted 16 April 2019

Available online 18 April 2019

0926-3373/© 2019 Elsevier B.V. All rights reserved.

$\text{CuFe}_2\text{O}_4$  nanoparticles are prone to agglomeration, which dramatically decreases their specific surface area and accessible reactive sites [23]. Various strategies, such as fabricating porous catalysts and anchoring nanoparticles on substrate materials, have been investigated for preventing the agglomeration of  $\text{CuFe}_2\text{O}_4$  nanoparticles. For example, Wang et al. [24] used the template to synthesize mesoporous  $\text{CuFe}_2\text{O}_4$  by a nanocasting strategy. Yao et al. [25] and Xu et al. [26] reported the synthesis of  $\text{CuFe}_2\text{O}_4$ /reduced graphene oxide which was applied to activate PMS and  $\text{H}_2\text{O}_2$ . Zhang et al. [27] immobilized nano-scaled  $\text{CuFe}_2\text{O}_4$  on carbon nanotubes and used for persulfate activation. However, the largely consumed high-cost template and supports would limit their practical application in the field of wastewater reclamation. Thus, it is important to explore an economical method for fabricating highly dispersive  $\text{CuFe}_2\text{O}_4$  nanoparticles.

Nowadays, natural minerals have been extensively utilized as supports of nanocatalysts due to their low cost, chemical stability and easy reusability [28,29]. Kaolinite, as one of natural minerals, displayed a two-dimensional lamellar structure and possessed abundant aluminum hydroxyl groups and permanent negative charge [30]. The two-dimensional lamellar structure should be a suitable platform for the graft of  $\text{CuFe}_2\text{O}_4$  nanoparticles. Abundant aluminum hydroxyl groups and permanent negative charge prevented the self-agglomeration of  $\text{CuFe}_2\text{O}_4$  nanoparticles via moderating their crystallization on the surface of kaolinite. Moreover, the aluminum abundant hydroxyl groups could be accounted as reactive sites for PMS activation [31]. Taking into account of these factors, anchoring  $\text{CuFe}_2\text{O}_4$  nanoparticles on the surface of kaolinite is expected to be an economical and efficient PMS catalyst for decomposition of refractory organic contaminants.

This work reports, for the first time, the synthesis and characterization of  $\text{CuFe}_2\text{O}_4$  nanoparticles anchored on the surface of kaolinite followed by the evaluation of the aforementioned catalyst for PMS activation and degradation of bisphenol A in water. The crystal phase, morphology, specific surface area, pore structure and surface chemical states of kaolinite, bare  $\text{CuFe}_2\text{O}_4$  and  $\text{CuFe}_2\text{O}_4$ /kaolinite composites were systematically investigated. The enhancement of PMS activation efficiency, stability and reusability of 40%- $\text{CuFe}_2\text{O}_4$ /kaolinite composite were explored as well. The effects of various operating parameters on the activation efficiency for PMS were further studied in detail. In addition, the potential reaction mechanisms for the activation of PMS by 40%- $\text{CuFe}_2\text{O}_4$ /kaolinite composite were proposed based on quenching experiments, electron spin resonance (ESR), X-ray photoelectron spectroscopy (XPS) and attenuated total reflectance-Fourier transform infrared spectra (ATR-FTIR) analysis. The possible degradation pathway of BPA was proposed via monitoring the transformation products.

## 2. Experimental methods

### 2.1. Materials

The kaolinite used in our study was obtained from Jiangsu province, China, and its elemental composition is displayed in Table S2. Bisphenol A ( $\text{C}_{15}\text{H}_{16}\text{O}_2$ , BPA), peroxymonosulfate ( $2\text{KHSO}_5\cdot\text{KHSO}_4\cdot\text{K}_2\text{SO}_4$ , PMS), and 5,5-Dimethyl-1-pyrroline *N*-oxide ( $\text{C}_{16}\text{H}_{11}\text{NO}$ , DMPO) were purchased from Sigma-Aldrich Chemical Company. Copper nitrate hemi pentahydrate ( $\text{Cu}(\text{NO}_3)_2\cdot 2.5\text{H}_2\text{O}$ ), citric acid ( $\text{C}_6\text{H}_8\text{O}_7$ ), ferric nitrate nonahydrate ( $\text{Fe}(\text{NO}_3)_3\cdot 9\text{H}_2\text{O}$ ), potassium phosphate monobasic ( $\text{KH}_2\text{PO}_4$ ), sodium sulfate ( $\text{Na}_2\text{SO}_4$ ), sodium chloride ( $\text{NaCl}$ ), sodium hydrogencarbonate ( $\text{NaHCO}_3$ ), sodium hydroxide ( $\text{NaOH}$ ), hydrochloric acid ( $\text{HCl}$ ), ethanol ( $\text{C}_2\text{H}_6\text{O}$ , EtOH), and *tert*-butyl alcohol ( $\text{C}_4\text{H}_{10}\text{O}$ , TBA), which were all of analytical reagent grade ( $\geq 99.7\%$ ), were purchased from Sinopharm Chemical Reagent Co., Ltd (Beijing, China). Purified water (18 M $\Omega$  cm) obtained from a Milli-Q system was utilized throughout our experiments.

### 2.2. Preparation of $\text{CuFe}_2\text{O}_4$ /kaolinite hybrid catalysts

The x- $\text{CuFe}_2\text{O}_4$ /kaolinite (labeled as x-CF/K, x presented the weight ratio of  $\text{CuFe}_2\text{O}_4$  to  $\text{CuFe}_2\text{O}_4$ /kaolinite composite, x = 20%, 30%, 40%, 50%, and 60%) hybrid catalysts were synthesized by a citrate combustion method according to previous studies [32]. Typically, 1 g of kaolinite was dispersed into 60 mL of Milli-Q water with vigorous stirring for 2 h. Then the specified stoichiometric ratio of copper nitrate hemi pentahydrate and ferric nitrate nonahydrate were dissolved into the resultant suspension with continuous stirring for 1 h, followed by adding specific amount of citric acid. The obtained homogeneous suspension was stirred vigorously at 95 °C for 4 h towards the formation of sticky gel, and calcined at 400 °C for 2 h. Finally, the obtained brown products were ground, washed with Milli-Q water and ethanol, and dried in an oven at 60 °C for 10 h. The bare  $\text{CuFe}_2\text{O}_4$  was prepared by the same method as CF/K hybrid catalysts without adding kaolinite. The kaolinite was also calcined at 400 °C for 2 h for further characterization and degradation experiments and its elemental composition was listed in Table S2.

### 2.3. Characterization

The crystal phases of the synthesized composites were determined by X-ray diffraction (XRD, Bruker, Germany) operating at 40 kV and 40 mA with a  $\text{Cu-K}\alpha$  ( $\lambda = 0.154056$  nm) X-ray source. The surface morphology and elemental mappings were examined by field emission scanning electron microscope (FESEM, Hitachi, Japan) mounted with an energy dispersive spectra analysis (EDS) and high-resolution transmission electron microscope (HRTEM, Tecnai G2 F20, Japan) operating at 200 kV. The Brunauer–Emmett–Teller (BET) specific surface areas and pore size distribution of as-prepared composites were derived from nitrogen absorption-desorption isotherms using a JW-BK nitrogen adsorption apparatus (JWGB Sci. &Tech, China) at the liquid nitrogen temperature. Attenuated total reflectance-Fourier transform infrared spectra (ATR-FTIR) were recorded using the Bruker Vertex 70 Hyperion 1000 spectrometer (Bruker, Germany). The generated reactive radicals were performed using the electron spin resonance (ESR, JES FA200, Japan), and the experimental conditions are as follows:  $\text{C}_0$  (BPA) = 50 mg L<sup>-1</sup>,  $\text{C}_0$  (PMS) = 5 mM,  $\text{C}_0$  (Catalyst) = 0.5 g L<sup>-1</sup>,  $\text{C}$  (DMPO) = 5 mM, and initial pH = 7.0. The changes of elemental composition and chemical oxidation states on the surface of as-prepared composites were conducted on an ESCALAB 250 spectrometer equipped with an Al K $\alpha$  source, and the binding energies of the composing elements were calibrated by C 1s (284.80 eV). The total organic carbon (TOC) was evaluated by a TOC-L analyzer (Shimadzu, Japan). After reaction, the suspension was filtered to remove the catalysts with a Millipore filter (pore size 0.22  $\mu\text{m}$ ), and the obtained solution was immediately adjusted to pH < 1 using 1 M of  $\text{H}_2\text{SO}_4$ , which was further used to determine the dissolved ions by an inductively coupled plasma mass spectrometry (ICP-MS, Agilent 8800, USA). The residual PMS was evaluated by the iodometric titration method [31].

### 2.4. Experimental procedure

Batch experiments were carried out in a 50 mL of round polypropylene copolymer centrifuge tubes, covered with a circular cover, and rotated by a rotating reactor with a low rotational rate (30 rpm) at room temperature. 1.0 M of NaOH and 1.0 M of  $\text{HNO}_3$  were used to adjust the initial pH. A specified kaolinite, bare  $\text{CuFe}_2\text{O}_4$  and x-CF/K hybrid catalyst were initially dispersed into 30 mL of BPA aqueous solution, and the resultant suspension was rotated for 10 min to ensure the establishment of an adsorption/desorption equilibrium between catalyst and target compound (Fig. S1). Then, a certain dose of PMS solution was added into the suspension. Once the BPA degradation was initiated, 0.5 mL of suspension was sampled and quenched by 0.5 mL of methanol at the given time intervals, and then filtered to remove the

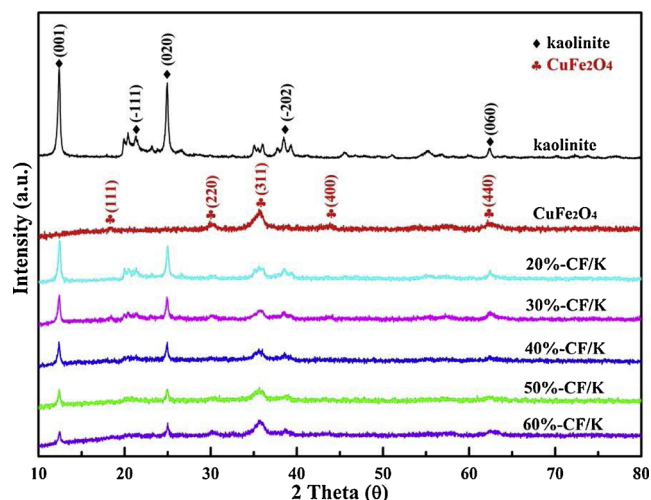


Fig. 1. XRD spectra of kaolinite, bare  $\text{CuFe}_2\text{O}_4$  and x-CF/K composites ( $x = 20\%$ ,  $30\%$ ,  $40\%$ ,  $50\%$ , and  $60\%$ ).

catalysts with a Millipore filter (pore size  $0.22\ \mu\text{m}$ ). All the BPA degradation experiments were conducted in triplicate.

After batch experiment, the suspension was filtered, washed with Milli-Q water and ethanol, and dried in an oven at  $60\ ^\circ\text{C}$  for 10 h. The obtained product was further used to explore the reusability of catalyst.

## 2.5. Analytical methods

The concentration of BPA was determined using a high performance liquid chromatography (HPLC, LC-20A Shimadzu, Japan) equipped with a UV detector at a wavelength of 220 nm. A welchrom  $4.6 \times 250\ \text{mm}$  XB-C18 column was utilized as the stationary phase and the isocratic mobile phase was composed of 60% of acetonitrile and 40% of Milli-Q water. The sample injection volume was  $100\ \mu\text{L}$ , and the flow rate was  $1\ \text{mL min}^{-1}$ .

The transformation products from BPA degradation were analyzed by using an electrospray ionization mass spectrometry (ESI-MS, MICROTOF-QII Bruker, Germany). The full-scan spectra were measured

with a scan range of  $m/z$  50–400 in a negative mode. The capillary voltage and pressure of nebulizer were 3000 V and 0.4 bar, respectively. The operating temperature was  $180\ ^\circ\text{C}$ , and the flow rate of dry gas was  $2.0\ \text{L min}^{-1}$ .

## 3. Results and discussion

### 3.1. Characterization of x-CF/K hybrid catalysts

The crystalline phases of kaolinite, bare  $\text{CuFe}_2\text{O}_4$  and x-CF/K hybrid catalysts were obtained by XRD and the results are presented in Fig. 1. The diffraction peaks of kaolinite located at  $12.44^\circ$  (001),  $23.74^\circ$  ( $-111$ ),  $24.98^\circ$  (020),  $38.48^\circ$  ( $-202$ ) and  $62.48^\circ$  (060) were readily indexed to triclinic kaolinite (JCPDS No. 14-0164) [33]. With respect to bare  $\text{CuFe}_2\text{O}_4$ , the diffraction peaks at  $18.51^\circ$  (111),  $30.17^\circ$  (220),  $35.64^\circ$  (311),  $43.04^\circ$  (400), and  $62.77^\circ$  (440) matched well with the cuprospinel phase ( $\text{CuFe}_2\text{O}_4$ , JCPDS No.25-0283) [34] without impurity peaks, revealing the good crystallinity of bare  $\text{CuFe}_2\text{O}_4$ . All the x-CF/K hybrid catalysts presented two-phase composition: kaolinite and  $\text{CuFe}_2\text{O}_4$ . With the increase of  $\text{CuFe}_2\text{O}_4$  component in CF/K composite, the intensities of diffraction peaks indexed to bare  $\text{CuFe}_2\text{O}_4$  increase gradually. No impurity phases were detected in the x-CF/K hybrid catalysts, confirming the high purity of these composites.

The morphology and microstructure of kaolinite, bare  $\text{CuFe}_2\text{O}_4$  and x-CF/K hybrid catalysts were examined by FESEM, TEM and HRTEM. The stacking sheets with smooth and well-defined edge were observed in the SEM image of kaolinite as shown in Fig. 2a. This lamellar structure is favorable for the uniform and stable anchoring of  $\text{CuFe}_2\text{O}_4$  nanoparticles in the synthesis process. The bare  $\text{CuFe}_2\text{O}_4$  particles resulting from the sol-gel combustion procedure are severely agglomerated (Fig. 2b). Interestingly, as for 40%-CF/K composite, the surface of kaolinite sheets became rough (Fig. 2c), suggesting the successful distribution and immobilization of  $\text{CuFe}_2\text{O}_4$  nanoparticles on the surface of kaolinite. Additionally, the EDS mapping images (Fig. 2d) clearly revealed that the Cu, Fe, Si, Al and O were uniformly distributed throughout the 40%-CF/K composite, further confirming the even immobilization of  $\text{CuFe}_2\text{O}_4$  nanoparticles on the surface of kaolinite.

TEM, HRTEM and SAED were applied to further investigate the morphology and microstructure of as-prepared samples as depicted in

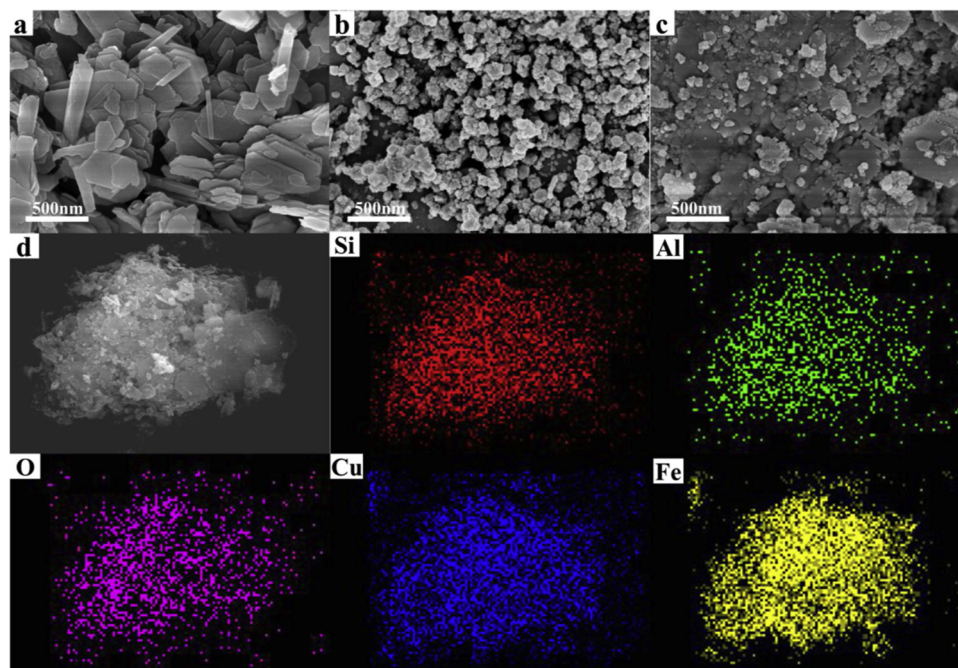
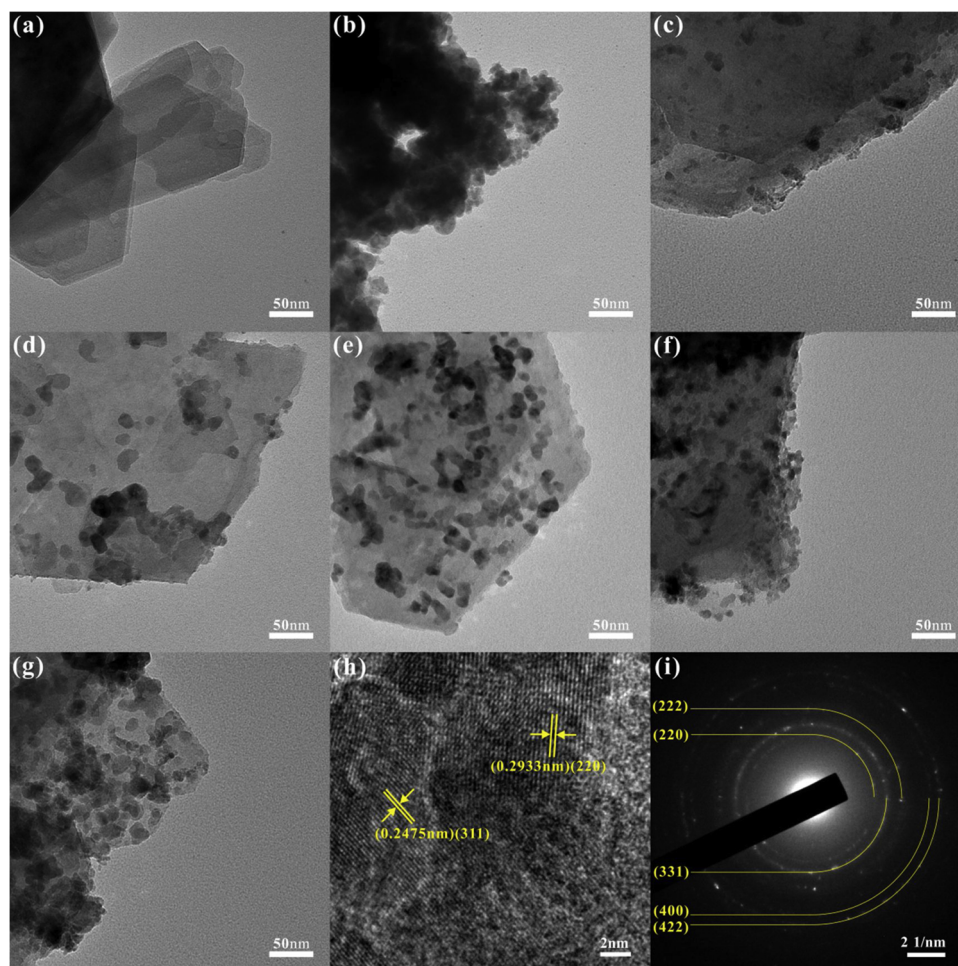


Fig. 2. SEM images of (a) kaolinite, (b) bare  $\text{CuFe}_2\text{O}_4$ , (c) 40%-CF/K composite, (d) EDS spectra as element mapping of Si, Al, O, Cu and Fe for 40%-CF/K composite.





**Fig. 3.** TEM images of (a) kaolinite, (b) bare  $\text{CuFe}_2\text{O}_4$ , (c)–(g) x-CF/K composite ( $x = 20\%$ ,  $30\%$ ,  $40\%$ ,  $50\%$ , and  $60\%$ ), (h) HRTEM images and (i) SAED pattern of 40%-CF/K composite.

**Fig. 3.** The agglomerated  $\text{CuFe}_2\text{O}_4$  nanoparticles and the stacking kaolinite sheets with smooth and well-defined edges are clearly seen in Fig. 3a and b. As for 40%-CF/K composite,  $\text{CuFe}_2\text{O}_4$  nanoparticles with the diameter of 10–20 nm were evenly distributed and anchored on the surface of kaolinite sheets (Fig. 3e). Additionally, the TEM images of x-CF/K composites (Fig. 3c–g) demonstrated that only a few  $\text{CuFe}_2\text{O}_4$  nanoparticles anchored on the surface of kaolinite at low  $\text{CuFe}_2\text{O}_4$  content ( $x < 40\%$ ), while significant agglomeration of  $\text{CuFe}_2\text{O}_4$  nanoparticles emerged on the surface of kaolinite sheets once  $x > 40\%$ , resulting in the decrease of accessible reactive sites. Fig. 3d shows a typical HRTEM image of 40%-CF/K composite with lattice fringe spacing of 0.248 nm and 0.293 nm, which can be indexed to the (311) and (220) planes of  $\text{CuFe}_2\text{O}_4$ , respectively [24]. Clear five-fold symmetric diffraction rings observed in the corresponding SAED pattern also demonstrated (Fig. 3g) the crystalline structure of  $\text{CuFe}_2\text{O}_4$  [35]. These results were well matched with those derived from SEM and XRD.

The pore textures of heterogeneous catalysts are important factors for their number of reactive sites and adsorption capacities, which play significant roles on the rate of degradation of target contaminants. The porous structure properties of kaolinite, bare  $\text{CuFe}_2\text{O}_4$ , and x-CF/K hybrid catalysts are displayed in Figs. 4, S2 and Table S3. All isotherm curves are of type IV adsorption branch with a typical  $\text{H}_3$  hysteresis loop, revealing the mesoporous structure of as-prepared samples (Figs. 4a and S2a) [36]. Compared to kaolinite, bare  $\text{CuFe}_2\text{O}_4$ , and other CF/K composites, the 40%-CF/K composite exhibited the highest specific surface area, largest pore volume, and smallest average pore diameter (Table S3 and Fig. S2b). Moreover, the pore size distribution

of 40%-CF/K composite was mainly in the range from 2 to 6 nm, much smaller than that of kaolinite and bare  $\text{CuFe}_2\text{O}_4$ . These specific pore structures would be favorable for the adsorption and migration of BPA molecules [37].

The surface characteristics of bare  $\text{CuFe}_2\text{O}_4$  and 40%-CF/K composite were elucidated by XPS analysis. The signals of Cu, Fe, Si, Al, O and C elements were detected in the survey spectra of 40%-CF/K composite (Fig. 5a). The observation of C element was attributed to adventitious contaminants. In the O1s spectra of bare  $\text{CuFe}_2\text{O}_4$ , the peaks centered at 529.9 eV and 531.4 eV were attributed to the lattice oxygen and surface hydroxyl groups, respectively (Fig. 5b) [38]. For the O1s of 40%-CF/K composite, a slight shift of the lattice oxygen peak might be due to the generation of new bonds between kaolinite and  $\text{CuFe}_2\text{O}_4$  nanoparticles. The higher peak intensity of hydroxyl groups revealed that the surface of 40%-CF/K composite possessed more hydroxyl groups owing to the introduction of kaolinite with abundant hydroxyls. On the one hand, the enhancement of hydroxyl groups could accelerate the dispersion of catalysts in aqueous system, further increasing the number of accessible reactive sites and enhancing the mass transfer of target contaminants. This result was well in accordance with the zeta potential analysis (Fig. S3). On the other hand, the hydroxyl groups on the surface of kaolinite could activate PMS and generate reactive radicals, which has been determined in our previous study [31]. Al 2p, Si 2p, Cu 2p and Fe 2p spectra of kaolinite, bare  $\text{CuFe}_2\text{O}_4$  and 40%-CF/K composite were further compared to determine the chemical coordination between kaolinite and  $\text{CuFe}_2\text{O}_4$  nanoparticles. In contrast to kaolinite, a pristine peak at 77.1 eV was observed in Al 2p



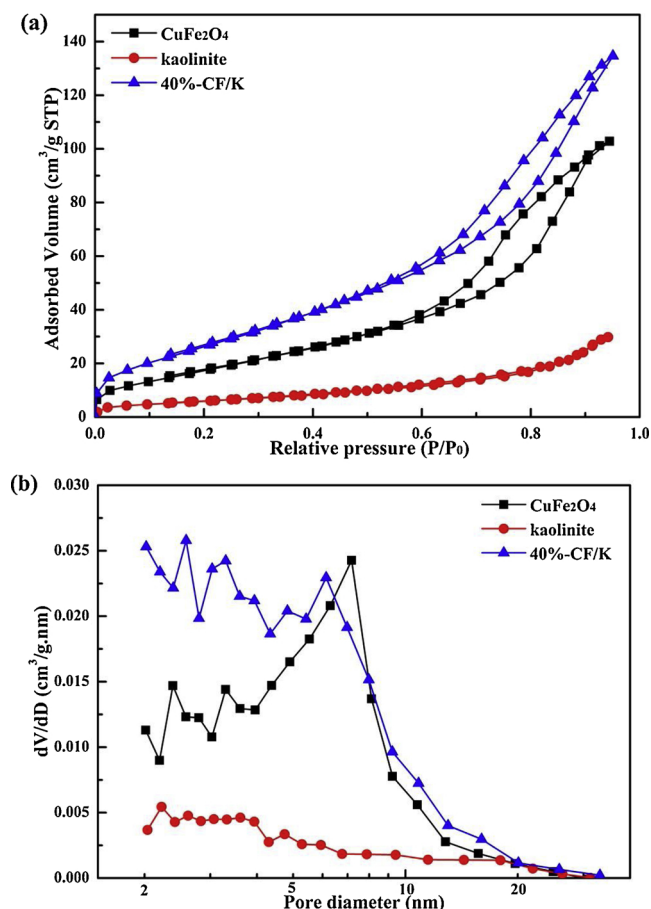


Fig. 4. (a) Nitrogen adsorption and desorption isotherms and (b) BJH pore size distribution plots for kaolinite, bare CuFe<sub>2</sub>O<sub>4</sub> and 40%-CF/K composite.

spectra (Fig. 5e) of 40%-CF/K composite, while nearly no difference can be detected in Si 2p spectra (Fig. 5f), suggesting the formation of Fe–O–Al or Cu–O–Al bond between CuFe<sub>2</sub>O<sub>4</sub> nanoparticles and kaolinite. There is no difference between Cu 2p (Fig. 5c) of bare CuFe<sub>2</sub>O<sub>4</sub> and 40%-CF/K composite. However, a slight shift towards higher binding energy could be monitored in Fe 2p spectra along with the immobilization of CuFe<sub>2</sub>O<sub>4</sub> nanoparticles on kaolinite. These results further revealed the generation of Fe–O–Al bond, which would be favorable for the chemical stability and reusability of CuFe<sub>2</sub>O<sub>4</sub> nanoparticles.

### 3.2. The catalytic activity of as-prepared samples

The data of BPA degradation in various systems are displayed in Fig. 6. It is clear in Fig. 6 that the 40%-CF/K composite presented higher adsorption capacity (12%) than kaolinite (6%) and bare CuFe<sub>2</sub>O<sub>4</sub> (4%). Around 13% of BPA could be removed by using kaolinite to catalyze PMS. With the addition of bare CuFe<sub>2</sub>O<sub>4</sub> to activate PMS, a rapid BPA degradation was recorded and even faster degradation rate was observed in the case of 40%-CF/K composite. Furthermore, the BPA degradation data in various systems were fitted well with the pseudo-first order kinetic model (Table S4). The reaction rate constant (*k*) values of BPA degradation were evaluated to be 0.0012, 0.0155 and 0.0589 min<sup>−1</sup> for kaolinite, bare CuFe<sub>2</sub>O<sub>4</sub> and 40%-CF/K composite, respectively, demonstrating that the CuFe<sub>2</sub>O<sub>4</sub> nanoparticles in 40%-CF/K composite dominated the PMS activation.

In addition, the influence of CuFe<sub>2</sub>O<sub>4</sub> mass content in CF/K composites on BPA degradation was investigated (Fig. S4). The catalytic efficiency of 20%-CF/K composite was even lower than that of bare CuFe<sub>2</sub>O<sub>4</sub> due to the low CuFe<sub>2</sub>O<sub>4</sub> content. The BPA degradation

efficiency dramatically increased with the increase of CuFe<sub>2</sub>O<sub>4</sub> content in CF/K composite from 20% to 40%. Then, the BPA degradation efficiency exhibited a smooth decrease trend when the CuFe<sub>2</sub>O<sub>4</sub> content in CF/K composite was excessive (*x* > 40%). This result could be attributed to the agglomeration of CuFe<sub>2</sub>O<sub>4</sub> nanoparticles, leading to the decrease of adsorption capacity and accessible reactive sites.

Based on the results of aforementioned analyses, in contrast to bare CuFe<sub>2</sub>O<sub>4</sub>, the 40%-CF/K composite with superior catalytic efficiency in PMS activation could be explained as follows: (i) its higher specific surface area and larger pore volume accelerated the adsorption and migration of BPA molecules; (ii) the abundant hydroxyl groups not only contributed to PMS decomposition, but also promoted the probability of contact between BPA molecules with catalysts via accelerating dispersion of catalysts in BPA aqueous system; (iii) the uniform immobilization of CuFe<sub>2</sub>O<sub>4</sub> nanoparticles on the surface of kaolinite resulted in the increase of accessible reactive sites.

### 3.3. Stability and reusability of as-prepared sample

The stability and reusability of 40%-CF/K composite are essential for its practical application. It was observed in Fig. 7 that the 40%-CF/K composite still maintained excellent catalytic activity after successively used for 5 times. The potential change of 40%-CF/K composite after five cycles was measured by XRD, SEM, TEM and FTIR. The XRD spectra of used catalyst showed no apparent changes as compared with those of fresh catalyst (Fig. S5). The similar phenomenon was also observed in TEM and SEM images of fresh and used 40%-CF/K composite (Figs. S6 and S7). The slight decrease of peak intensity in the FTIR spectra was ascribed to the leached metal ions after five cycles (Fig. S8). The leaching of metal ions was further investigated during the oxidation process and results are presented in Table S5 (the initial PMS concentration = 0.5 mM, the dosage of catalyst = 0.5 g/L, initial pH = 7.0). In 40%-CF/K composite/PMS system, the concentration of leached copper and ferric was around 0.27 and 0.01 mg/L respectively, which was lower than the recommended limits in reclaimed water. In contrast to bare CuFe<sub>2</sub>O<sub>4</sub>, 40%-CF/K composite presented lower leaching of ions in the catalyst/PMS oxidation system, which might be attributed to the generation of Fe–O–Al bond between CuFe<sub>2</sub>O<sub>4</sub> and kaolinite. This phenomenon was well consistent with the results obtained from BET and XPS analyses. In addition, the copper and ferric ions with the same concentration of released ions in 40%-CF/K/PMS system were utilized to carry out homogeneous activation experiments. The results (Fig. S9) proved that PMS decomposition was dominated by heterogeneous activation mechanism, similar to the previous study [39].

### 3.4. Reactive species and possible mechanisms

#### 3.4.1. Identification of reactive species

The PMS decomposition tests showed that around 6% of PMS was decomposed after reaction for 60 min in the absence of 40%-CF/K composite, while the PMS decomposition was up to 85% (Fig. S10). This phenomenon revealed that 40%-CF/K composite significantly accelerated the decomposition of PMS to generate involved reactive radicals. Generally, sulfate, hydroxyl and peroxy-sulfate radicals might be considered as involved reactive radicals in catalyst/PMS oxidation system. The BPA degradation responsible for SO<sub>5</sub><sup>•−</sup> generated from the oxidation of sulfite radical could be neglected because of its lower oxidation potential (*E*<sup>°</sup>(SO<sub>5</sub><sup>•−</sup>) = 0.81 V) [40,41]. To determine the presence of SO<sub>4</sub><sup>•−</sup> and <sup>•</sup>OH in the 40%-CF/K composite/PMS oxidation system, ESR experiments were conducted with DMPO as the spin-trapping agent. No apparent signal was detected in the presence of PMS only, proving that there was nearly no SO<sub>4</sub><sup>•−</sup> or <sup>•</sup>OH in the bare PMS solution (Fig. 8a). After the addition of 40%-CF/K composite for 2.5 min, a four-line peaks was detected in the ESR spectra, with the relative intensities of 1:2:2:1 and the hyperfine splitting constants of *a<sub>N</sub>*

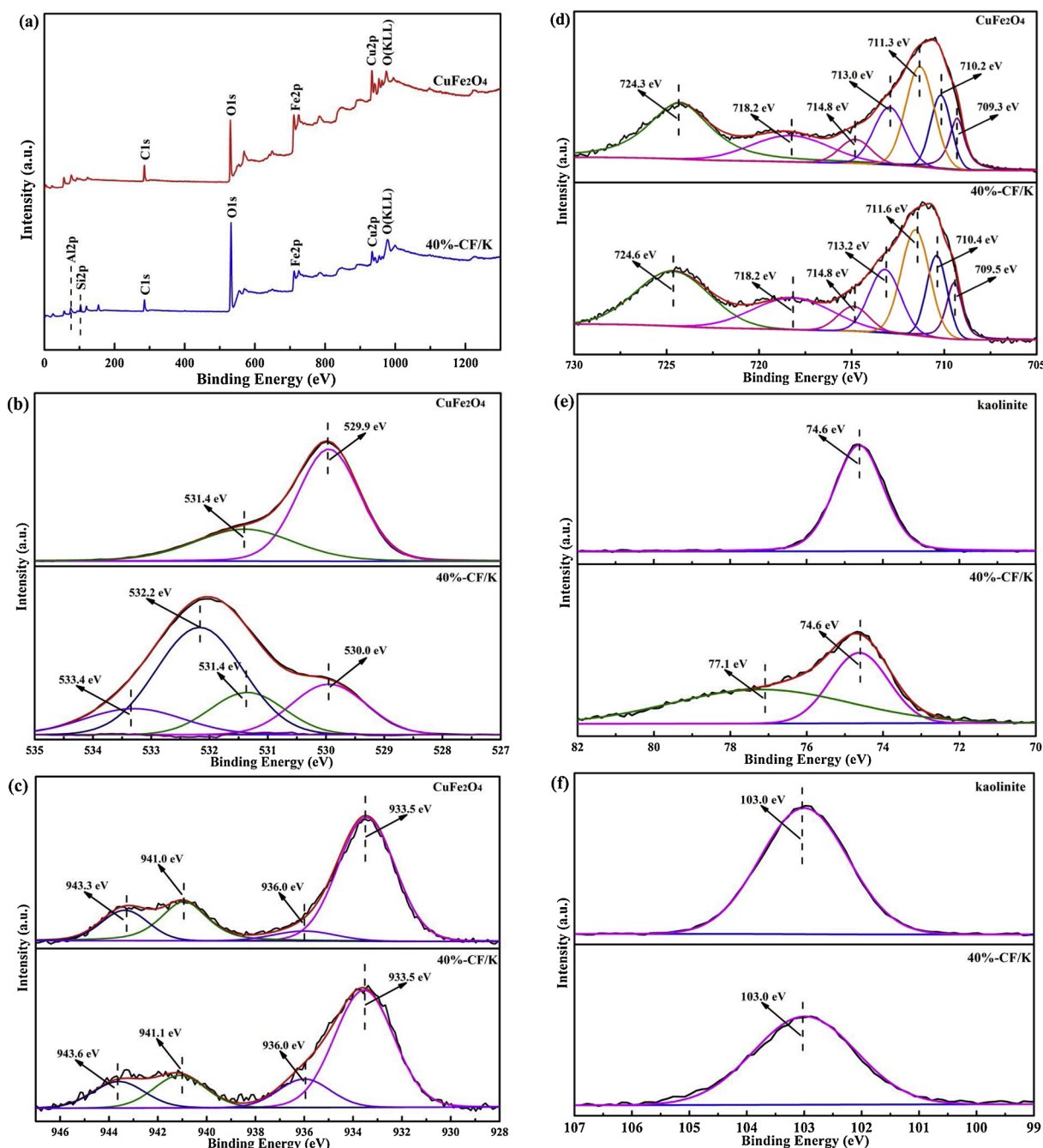


Fig. 5. XPS spectra of (a) survey, (b) O1s, (c) Cu 2p, (d) Fe 2p, (e) Al 2p and (f) Si 2p for bare CuFe<sub>2</sub>O<sub>4</sub> and 40%-CF/K composite.

$= a_H = 14.9$  G, which was matched well with the spectra of DMPO/ $\cdot$ OH adduct [42]. The characteristic spectra of DMPO/ $\text{SO}_4^{\cdot-}$  adduct generated from the sulfate radical was observed as well [43]. However, the relative intensity of the DMPO/ $\text{SO}_4^{\cdot-}$  adduct spectra was much weaker than that of DMPO/ $\cdot$ OH adduct spectra, which might be attributed to the rapid consumption of  $\text{SO}_4^{\cdot-}$  via reacting with BPA or hydroxyl ion (Eq. (1)) [44]. Additionally, the relative intensities of ESR spectra became stronger with the increase of reaction time. The ESR results confirmed that both  $\cdot$ OH and  $\text{SO}_4^{\cdot-}$  were constantly generated and contributed to BPA degradation in the 40%-CF/K composite/PMS oxidation system.



Furthermore, to examine the predominant radical species in the 40%-CF/K composite/PMS oxidation system, radical quenching experiments

were carried out. The alcohols containing  $\alpha$ -hydrogen, such as ethanol (EtOH), can rapidly scavenge both  $\cdot$ OH ( $k = (1.2\text{--}2.8) \times 10^9 \text{ mol L}^{-1} \text{ s}^{-1}$ ) and  $\text{SO}_4^{\cdot-}$  ( $k = (1.6\text{--}7.7) \times 10^7 \text{ mol L}^{-1} \text{ s}^{-1}$ ) [45]. The *tert*-butyl alcohol (TBA) as one of the alcohols without  $\alpha$ -hydrogen can readily scavenge  $\cdot$ OH ( $k = (3.8\text{--}7.6) \times 10^8 \text{ mol L}^{-1} \text{ s}^{-1}$ ) as well, and its reaction constant is over 1000-fold higher than that for  $\text{SO}_4^{\cdot-}$  [45]. Hence, EtOH and TBA were applied as scavengers in radical quenching experiments to differentiate the contribution between  $\text{SO}_4^{\cdot-}$  and  $\cdot$ OH. As presented in Fig. 8b, around 97% of BPA was removed in the absence of scavengers. When 0.1 M TBA was added, the BPA degradation efficiency slightly decreased to around 85%, and no apparent difference was observed with the increase of TBA dosage to 0.5 M. In contrast, the BPA degradation efficiency dramatically decreased to 37% in the presence of 0.1 M of EtOH, and the inhibition effect was more remarkable when the EtOH dosage had increased to 0.5 M. These results determined that  $\text{SO}_4^{\cdot-}$  played the dominant role for BPA degradation in the

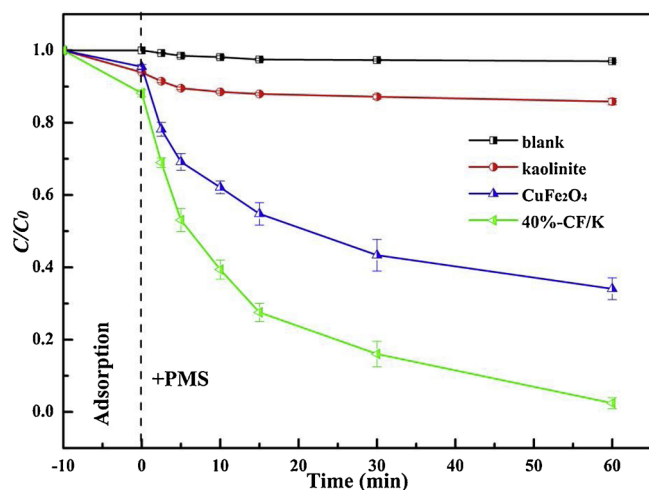


Fig. 6. BPA degradation with various catalysts in PMS oxidation system. Conditions:  $C_0$  (BPA) = 50 mg L<sup>-1</sup>;  $C_0$  (PMS) = 0.5 mM;  $C_0$  (Catalyst) = 0.5 g L<sup>-1</sup>; initial pH = 7.0; T = 298 K.

40%-CF/K composite/PMS oxidation system, and the presence of  $\cdot\text{OH}$  in the oxidation system might be generated from the reaction of  $\text{SO}_4^{\cdot-}$  with the hydroxyl ion.

### 3.4.2. Sulfate radical generation mechanism

The sulfate radical generation mechanism based on copper active sites in 40%-CF/K composite might be responsible for leached copper ion. We speculated that high-valence metal ion (Cu(III)) was generated with the decomposition of PMS. The presence of high-valence metal ion (Cu(III)) is difficult to identify because of its highly unstable properties. Interestingly, the high-valence metal ion (Cu(III)) possessed higher binding capacity with hydroxyl groups because of its smaller ionic radii [46]. In the 40%-CF/K composite/PMS oxidation system, the electron density of hydroxyl groups generated from the dissociation of water would shift with the change of valence states of transition metals. The shift of the electron density of hydroxyl groups could be observed in situ spectroscopic analysis. Thus, the generation of high-valence metal ions during the oxidation process could be indirectly determined based on these theories. Furthermore, Zhang et al have proven the generation of high-valence metal ion (Cu(III)) in  $\text{CuFe}_2\text{O}_4$ /PMS oxidation system based on these theories [16].

ATR-FTIR tests were conducted during the oxidation process and results are depicted in Fig. 9. The absorption bands located at 1102 and

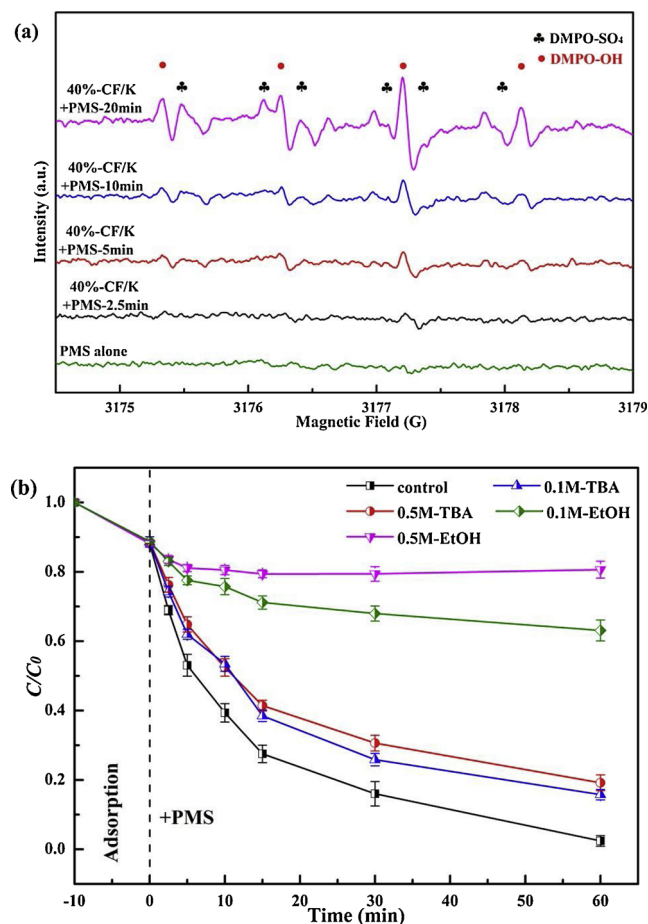


Fig. 8. (a) ESR spectra of bare PMS solution and 40%-CF/K composite/PMS oxidation system, Conditions:  $C_0$  (BPA) = 50 mg L<sup>-1</sup>;  $C_0$  (PMS) = 5 mM;  $C_0$  (Catalyst) = 0.5 g L<sup>-1</sup>; C (DMPO) = 5 mM; initial pH = 7.0; (b) Effect of radical scavengers on BPA degradation, Conditions:  $C_0$  (BPA) = 50 mg L<sup>-1</sup>;  $C_0$  (PMS) = 0.5 mM;  $C_0$  (Catalyst) = 0.5 g L<sup>-1</sup>; initial pH = 7.0; T = 298 K.

1247 cm<sup>-1</sup> in the spectra of PMS can be assigned to S–O bond stretching vibration of  $\text{SO}_4^{2-}$  and  $\text{HSO}_3^-$  respectively [47]. The relative intensity of peak at 1247 cm<sup>-1</sup> declined evidently in the case of 40%-CF/K composite, which is ascribed to the rapid decomposition of PMS. Furthermore, a blue-shift of 28 cm<sup>-1</sup> can be detected in the presence of 40%-CF/K composite, proving the generation of  $\equiv\text{Cu(II)}-(\text{HO})\text{OSO}_3^-$

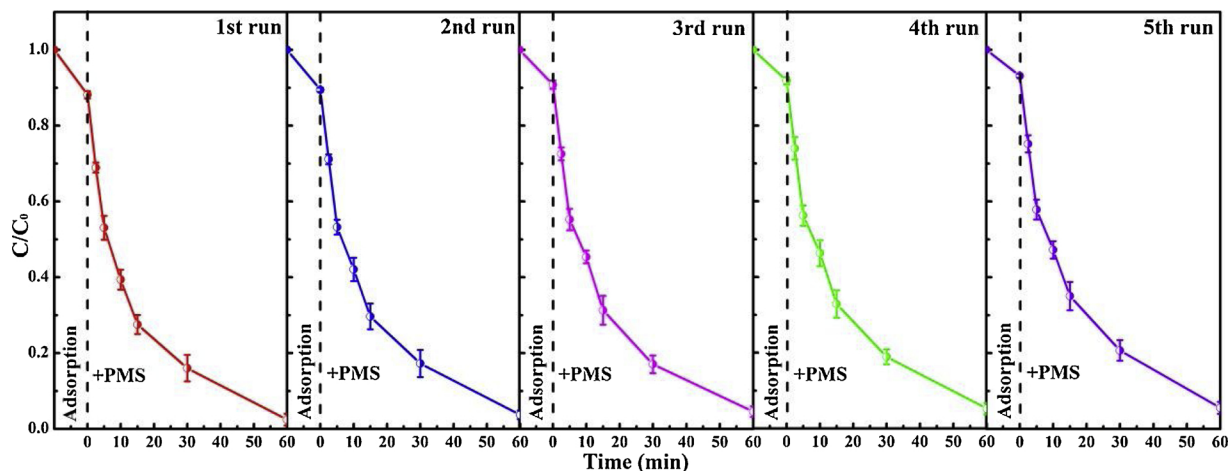


Fig. 7. BPA degradation in five consecutive runs by 40%-CF/K composite/PMS oxidation system. Conditions:  $C_0$  (BPA) = 50 mg L<sup>-1</sup>;  $C_0$  (PMS) = 0.5 mM;  $C_0$  (Catalyst) = 0.5 g L<sup>-1</sup>; initial pH = 7.0; T = 298 K.



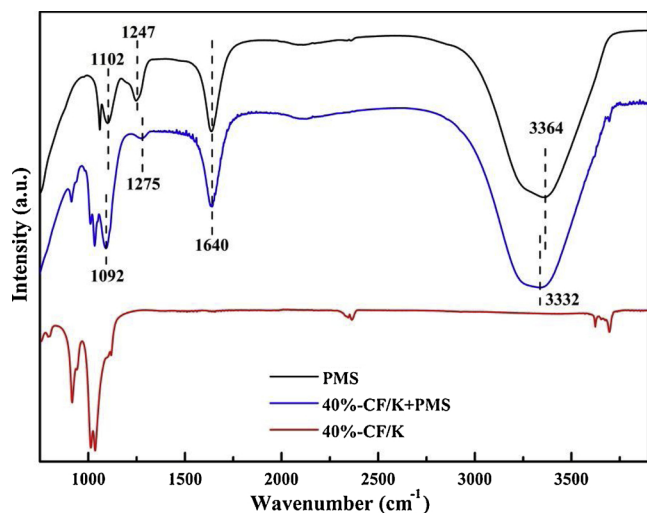
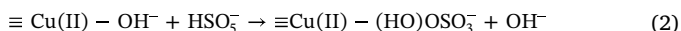
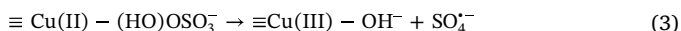


Fig. 9. ATR-FTIR spectra for PMS, 40%-CF/K composite and 40%-CF/K composite/PMS in water matrix.

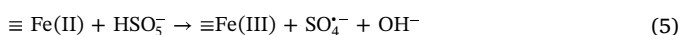
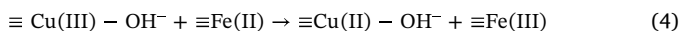
(Eq. (2)) on the surface of composite, which would increase the strength of S–O stretching bond [48].



Compared to the spectra of PMS, the absorption bands centered at  $1640 \text{ cm}^{-1}$  and  $3332 \text{ cm}^{-1}$  become broader in the presence of catalyst, indicating the promotion of surface hydroxyl groups, which could contribute to the strong hydroxylation on the surface of 40%-CF/K composite. Moreover, a red-shift of  $32 \text{ cm}^{-1}$  (from  $3364$  to  $3332 \text{ cm}^{-1}$ ) occurred during the oxidation process, demonstrating that the electron density of hydroxyl group shifted to the surface of 40%-CF/K composite due to the increase in the withdrawing capability of the catalyst surface. This result evidenced the presence of high-valence metal ion ( $\text{Cu(III)}$ ) during the generation process of sulfate radicals (Eq. (3)).



To further determine the reactive sites, the surface characteristics of fresh and used 40%-CF/K composite were characterized by XPS analysis and the results are presented in Fig. 10 and Table S6. The characteristic peaks assigned to Cu 2p, Fe 2p, O 1s, Si 2p and Al 2p were monitored in the survey scan of both fresh and used 40%-CF/K composite (Fig. 10a). After five cycles, the relative intensity of Cu 2p peak decreased slightly owing to the dissolution of copper during the oxidation process (Table S6). In the O 1s spectra, the relative intensity of peak assigned to the surface hydroxyl groups increased (Fig. 10b), which was in accordance with the result of ATR-FTIR. Nearly no peak shifting can be detected in the fresh and used Cu 2p spectra (Fig. 10c), unlike the observation of previous studies [32,49,50]. Moreover, the peak (at  $709.5 \text{ eV}$ ) intensity assigned to the  $\equiv \text{Fe(II)}$  decreased and a slight shift could be observed in the Fe 2p spectra, which could be ascribed to the oxidation of  $\equiv \text{Fe(II)}$  to  $\equiv \text{Fe(III)}$  (Fig. 10d) [49,51]. As the standard reduction potential of  $\equiv \text{Cu(III)}/\equiv \text{Cu(II)}$  ( $2.4 \text{ V}$ ) is much higher than that of  $\equiv \text{Fe(III)}/\equiv \text{Fe(II)}$  ( $0.77 \text{ V}$ ), we speculated that  $\equiv \text{Cu(III)} - \text{OH}^-$  might be reduced by the  $\equiv \text{Fe(II)}$  presented in the 40%-CF/K composite (Eq. (4)). In addition, the  $\equiv \text{Fe(II)}$  used to activate PMS might lead to the transformation of  $\equiv \text{Fe(II)}$  to  $\equiv \text{Fe(III)}$  in this system (Eq. (5)).



Our previous study has determined that the abundant hydroxyl groups of kaolinite can account as active sites for PMS decomposition, and the possible generation mechanism of reactive radicals have been proposed [31]. On the basis of the analysis of results above, the

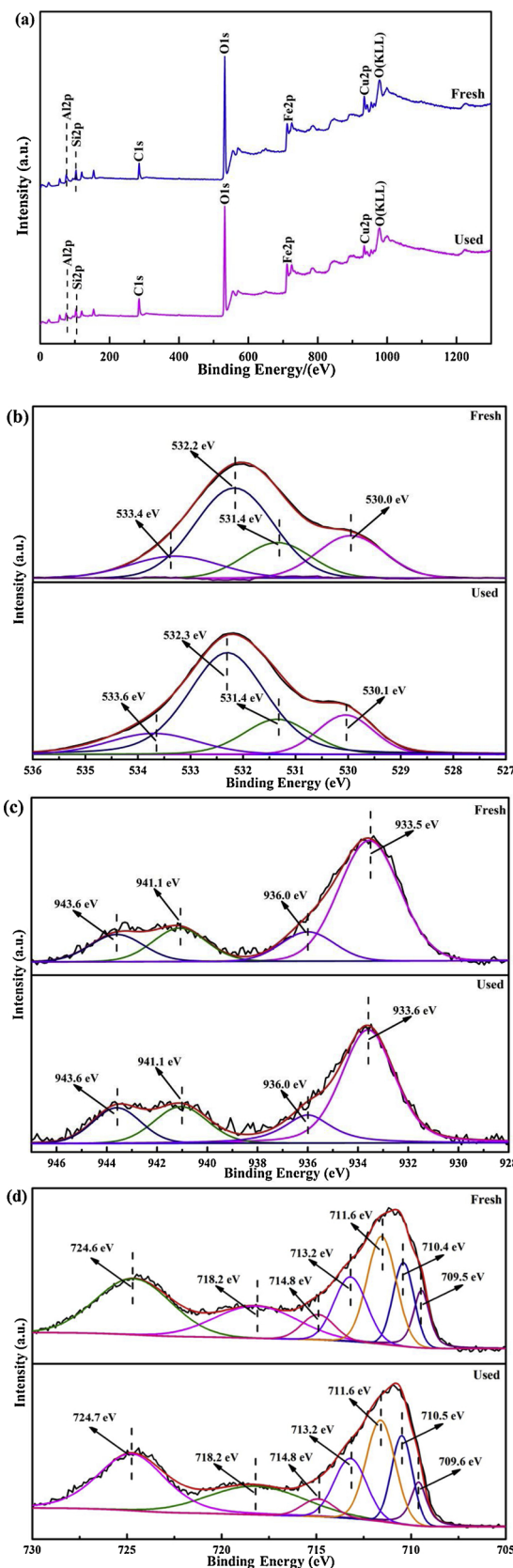
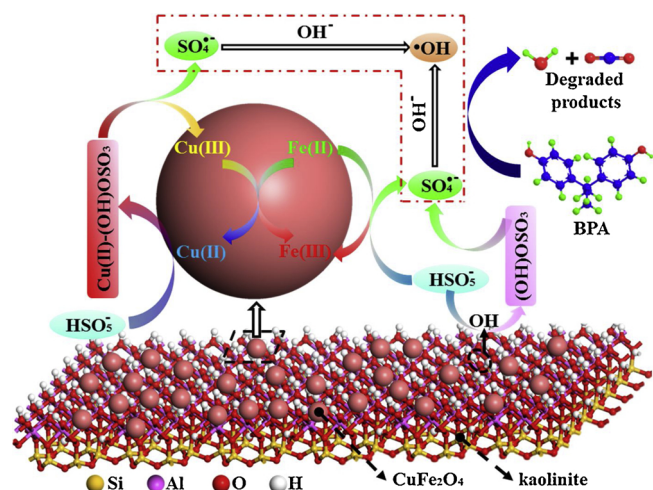


Fig. 10. XPS spectra of (a) survey, (b) O 1s, (c) Cu 2p, (d) Fe 2p for fresh and used 40%-CF/K composite.



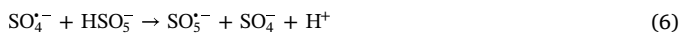
**Scheme 1.** Schematic of the radical generation mechanism and possible radicals' transfer routes.

catalytic mechanism for 40%-CF/K composite was proposed and is illustrated in [Scheme 1](#).

### 3.5. Influence of CF/K hybrid catalyst loading, PMS dosage, pH, and inorganic anions on BPA degradation

The influence of 40%-CF/K composite loading on BPA degradation was investigated and results are presented in [Fig. 11a](#). The degradation efficiency increased rapidly when the bare  $\text{CuFe}_2\text{O}_4$  loading was between 0.25–1.0 g/L, whereas no remarkable increase was observed in the range of 1.0–2.0 g/L. This result was probably attributed to the scavenging effect when excessive catalysts were used, similar to the results of several previous studies [[13,51](#)].

In addition, an increase of initial PMS concentration had a positive effect on BPA degradation efficiency within the range of 0.25 to 0.5 mM, whereas a dramatic decline was observed in the case of overdose (in the range of 0.5–2 mM) ([Fig. 11b](#)). This phenomenon might be ascribed to the scavenging of  $\text{SO}_4^{\bullet-}$  by the excessive  $\text{HSO}_5^-$  (Eq. (6)) [[51,52](#)].



The initial pH value is a significant parameter for the degradation of BPA in the PMS/catalysts oxidation system due to its influence on the generation of reactive radical species and the speciation of organic compounds [[53,54](#)]. When the PMS was oxidized along with the decomposition of BPA, pH value of the reaction suspension declined smoothly to around 3.6 in 60 min ([Fig. S11](#)). Prior to the addition of PMS, no obvious difference was observed on the adsorption capacity of catalyst in various initial pH values ([Fig. 11c](#)). With the addition of PMS, the 40%-CF/K composite presented appreciable BPA degradation efficiency in the initial pH values range of 5.0–9.1, and the optimal BPA degradation efficiency was obtained at pH of 7.0. The BPA degradation efficiency decreased significantly when the initial pH of solution was adjusted to strong acidic (3.3) and alkaline (10.6). It can be induced from the  $\text{pK}_a$  values of PMS ( $\text{pK}_{a1} < 0$  and  $\text{pK}_{a2} = 9.4$ ) that  $\text{HSO}_5^-$  was mainly presented in the PMS solution in the pH range of 0–9.4 [[13,16](#)]. The 40%-CF/K composite has a point of zero charge at pH = 4.7 ([Fig. S3](#)). At a strong acidic condition (pH = 3.3),  $\text{H}^+$  attached on the surface of  $\text{HSO}_5^-$  and generate H-bond with the O–O bond [[32](#)], and then  $\text{HSO}_5^-$  with positive charge would inhibit the interaction between PMS species and positively charged 40%-CF/K composite surface. As the initial pH value was increased to strong alkaline,  $\text{SO}_5^{2-}$  was formed in the solution, which might hinder its static interaction with 40%-CF/K composite surface.

In general, wastewater contains various inorganic anions (such as

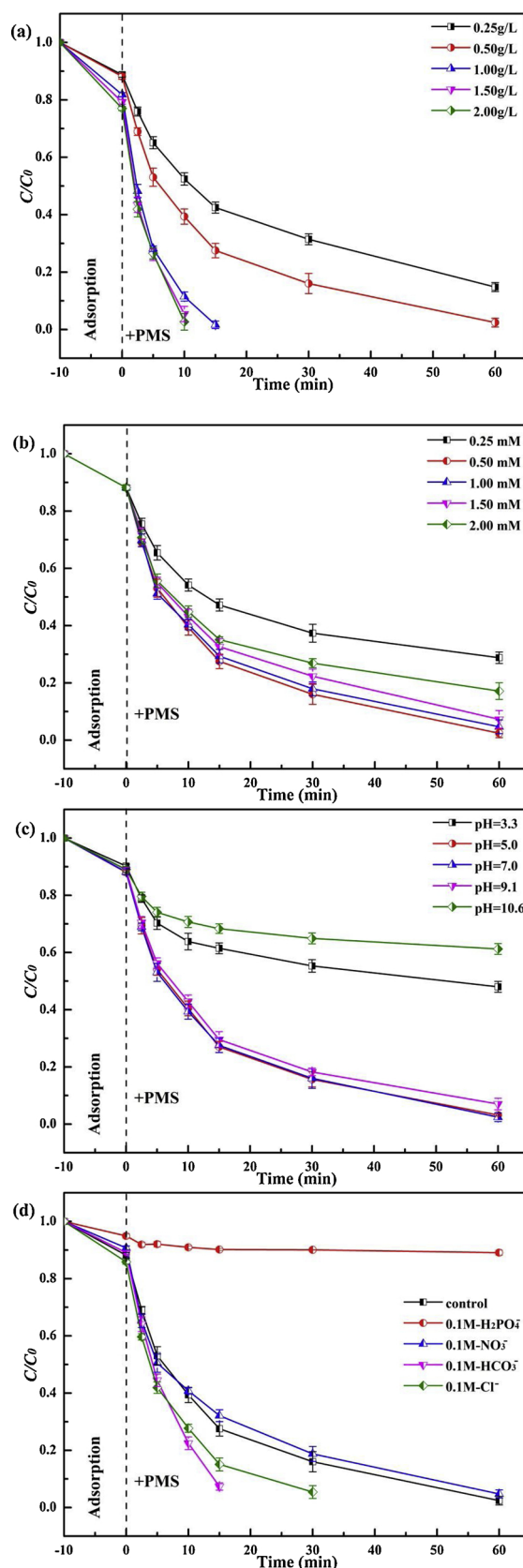


**Fig. 11.** Effects of (a) catalyst loading, (b) PMS dosages, (c) initial pH values and (d) inorganic anions on BPA degradation by 40%-CF/K composite/PMS oxidation system. General conditions:  $C_0$  (BPA) = 50 mg L<sup>-1</sup>;  $C_0$  (PMS) = 0.5 mM;  $C_0$  (Catalyst) = 0.5 g L<sup>-1</sup>; initial pH = 7.0; T = 298 K.

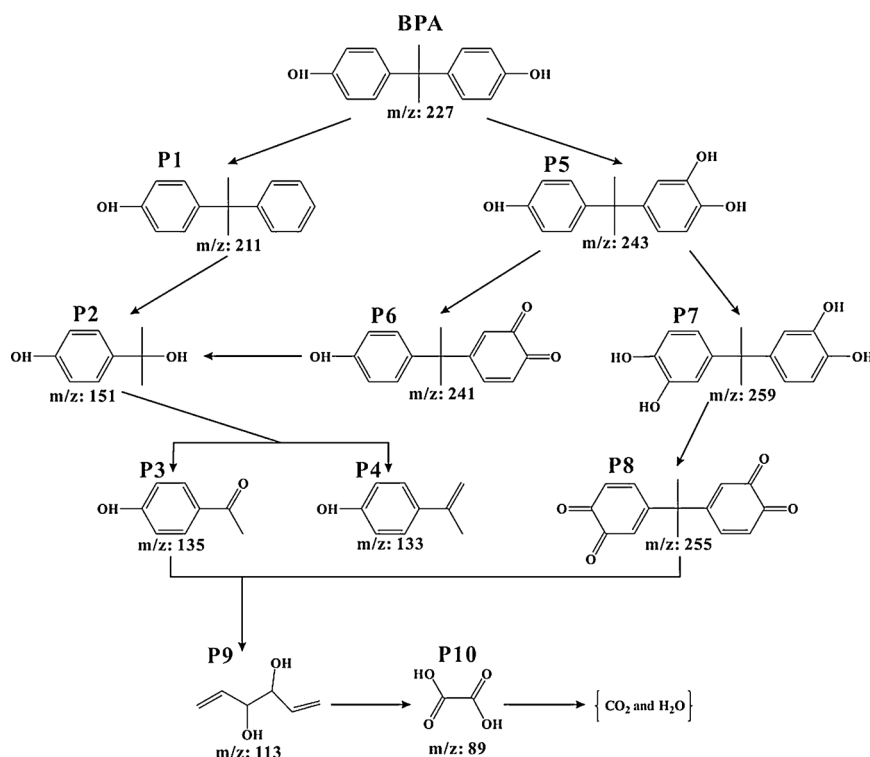
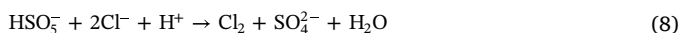


Fig. 12. Potential degradation pathway of BPA.

$\text{Cl}^-$ ,  $\text{NO}_3^-$ ,  $\text{H}_2\text{PO}_4^-$ ,  $\text{HCO}_3^-$ , etc.), which compete with target contaminants in the PMS oxidation system due to their reaction with radical species [14]. Compared to the oxidation system in the absence of inorganic anions, no significant impact on BPA degradation was observed with the addition of 0.1 M of  $\text{NO}_3^-$  (Fig. 11d). Previous study proved that dihydrogen phosphate ion ( $\text{H}_2\text{PO}_4^-$ ) could catalyze PMS [55]. However,  $\text{H}_2\text{PO}_4^-$  exhibited an inhibitory effect in 40%-CF/K/PMS oxidation system, much higher than the inhibition caused by 0.1 M of EtOH or TBA. This strong hindering phenomenon might be ascribed to decrease of reactive sites via chelating reactions during the PMS oxidation system [50]. The presence of chloride ion ( $\text{Cl}^-$ ) and bicarbonate ion ( $\text{HCO}_3^-$ ) in the oxidation system can accelerate the BPA degradation, and the acceleration effect of  $\text{HCO}_3^-$  was higher than that of  $\text{Cl}^-$ . The positive influence of bicarbonate ion ( $\text{HCO}_3^-$ ) on BPA degradation may be ascribed to the remarkable promotion of the generation of reactive oxygen species in the 40%-CF/K composite/PMS/ $\text{HCO}_3^-$  oxidation system [56,57]. According to Eqs. (7)–(10), chloride can react with  $\text{HSO}_5^-$  and  $\text{SO}_4^{\cdot-}$  to generate active chlorine or hypochlorous species.



The generated active chlorine species can combine with the unsaturated bonds of contaminants, producing adsorbable organic halides, which would be favorable for the transformation of target contaminants on the surface of catalysts [58,59]. We suspected that the generated active chlorine species might play a significant role in the 40%-CF/K composite/PMS/ $\text{Cl}^-$  oxidation system via accelerating the BPA transformation reactions.

### 3.6. Transformation products and potential degradation mechanisms

The transformation products of BPA in the 40%-CF/K composite/PMS system were monitored by ESI-MS analysis. As depicted in Fig. S12 and Table S7, 10 transformation products could be identified. Furthermore, the TOC degradation efficiency was investigated and the results are shown in Fig. S13. The TOC removal efficiency was around 55%, demonstrating high BPA mineralization in this system. Based on the mass-to-charge ratio ( $m/z$ ) of various products and the TOC results, the possible reaction pathway with three routes could be proposed (Fig. 12) [15,60–62]. First, the generated sulfate or hydroxyl radicals might attack the C–O bond via a dehydroxylation pathway resulting in the generation of P1 (4-Cumylphenol,  $m/z = 211$ ). After that, the electron-rich alkyl carbon would be attacked by the reactive radicals and converted to P2 (2-(4-hydroxyphenyl)-propanol-2-ol,  $m/z = 151$ ). Moreover, the hydroxyl radicals might attack the BPA aromatic ring, transforming to P5 (monohydroxylated-BPA,  $m/z = 243$ ) through the hydroxylation pathway, which is further converted to P6 (Quinone of monohydroxylated BPA,  $m/z = 241$ ), and sequentially oxidized into P7. Further attack on the tertiary hydroxyl leads to the formation of P3 (4-Hydroxyacetophenone,  $m/z = 135$ ) and P4 (p-isopropenyl phenol,  $m/z = 133$ ). The aromatic ring of P5 might further be attacked resulting in the formation of P7 (dihydroxylated BPA,  $m/z = 259$ ), which could be oxidized into P8 (quinone of dihydroxylated BPA,  $m/z = 255$ ). Ring-rupturing reactions could take place on P3, P4 and P8 in the presence of hydroxyl radicals and sulfate radicals resulting to the formation of P9 (divinyloxyethane,  $m/z = 113$ ) and P10 (ethanedioic acid,  $m/z = 89$ ) in sequence, and ultimately mineralized into  $\text{CO}_2$  and  $\text{H}_2\text{O}$ .

## 4. Conclusions

In summary, the CF/K composites with different content were successfully synthesized via a citrate combustion method, among which the 40%-CF/K composite presented the highest catalytic performance to activate PMS for BPA degradation, and its reaction rate constant value is around 5.5 times higher than that of bare  $\text{CuFe}_2\text{O}_4$ . These could be



ascribed to the higher specific surface area, larger pore volume, more hydroxyl groups, and more accessible reactive sites of 40%-CF/K composite. Moreover, the composite still retained excellent catalytic activity after successively used for 5 times, and presented the lower ionic release concentration due to the uniform immobilization of  $\text{CuFe}_2\text{O}_4$  nanoparticles on the surface of kaolinite with Fe–O–Al bond. Based on the results of XPS, ATR-FTIR, ESR and radical quenching experiments, the sulfate radical might be mainly generated through the oxidation of  $\text{Fe(II)}$  and  $\text{Cu(II)/Cu(III)}$  and  $\text{Cu(III)/Cu(II)}$  redox reaction, which played the predominant role for BPA degradation in 40%-CF/K composite/PMS oxidation system. In addition, the possible BPA degradation pathway was proposed through the evaluation of transformation products. This work would provide an innovative strategy via fabricating highly-efficient natural minerals-based catalysts to generate sulfate radicals from PMS for wastewater treatment.

## Acknowledgements

This work is supported by the Yueqi Funding Scheme for Young Scholars (China university of Mining & Technology, Beijing), Young Elite Scientists Sponsorship Program by CAST (2017QNRC001), Fundamental Research Funds for the Central Universities (2015QH01 and 2010YH10) and China Scholarship Council (CSC) (No. 201806430041). D. D. Dionysiou acknowledges support from the University of Cincinnati through a UNESCO co-Chair Professor position on “Water Access and Sustainability” and the Herman Schneider Professorship in the College of Engineering and Applied Sciences.

## Appendix A. Supplementary data

Supplementary material related to this article can be found, in the online version, at doi:<https://doi.org/10.1016/j.apcatb.2019.04.052>.

## References

- G.D. Bittner, C.Z. Yang, M.A. Stoner, Estrogenic chemicals often leach from BPA-free plastic products that are replacements for BPA-containing polycarbonate products, *Environ. Health* 13 (2014) 41–54.
- A. Schecter, N. Malik, D. Haffner, S. Smith, T.R. Harris, O. Paepke, L. Birnbaum, Bisphenol A (BPA) in U.S. food, *Environ. Sci. Technol.* 44 (2010) 9425–9430.
- A.V. Krishnan, P. Stathis, S.F. Permuth, L. Tokes, D. Feldman, Bisphenol-A: an estrogenic substance is released from polycarbonate flasks during autoclaving, *Endocrinology* 132 (1993) 2279–2286.
- S. Flint, T. Markle, S. Thompson, E. Wallace, Bisphenol A exposure, effects, and policy: a wildlife perspective, *J. Environ. Manage.* 104 (2012) 19–34.
- H. He, B. Huang, G. Fu, D. Xiong, Z. Xu, X. Wu, X. Pan, Electrochemically modified dissolved organic matter accelerates the combining photodegradation and biodegradation of 17 $\alpha$ -ethinylestradiol in natural aquatic environment, *Water Res.* 137 (2018) 251–261.
- W. Guo, W. Hu, J. Pan, H. Zhou, W. Guan, X. Wang, J. Dai, L. Xu, Selective adsorption and separation of BPA from aqueous solution using novel molecularly imprinted polymers based on kaolinite/ $\text{Fe}_3\text{O}_4$  composites, *Chem. Eng. J.* 171 (2011) 603–611.
- J. Sajiki, J. Yonekubo, Degradation of bisphenol-A (BPA) in the presence of reactive oxygen species and its acceleration by lipids and sodium chloride, *Chemosphere* 46 (2002) 345–354.
- A. Luca, R. Dantas, S. Esplugas, Study of  $\text{Fe(III)}$ -NTA chelates stability for applicability in photo-Fenton at neutral pH, *Appl. Catal. B: Environ.* 179 (2015) 372–379.
- M. Umar, F. Roddick, L. Fan, H.A. Aziz, Application of ozone for the removal of bisphenol A from water and wastewater—a review, *Chemosphere* 90 (2013) 2197–2207.
- A.H. Mady, M.L. Baynosa, D. Tuma, J.J. Shim, Facile microwave-assisted green synthesis of  $\text{Ag-ZnFe}_2\text{O}_4/\text{rGO}$  nanocomposites for efficient removal of organic dyes under UV- and visible-light irradiation, *Appl. Catal. B: Environ.* 203 (2017) 416–427.
- X. Dong, Z. Sun, X. Zhang, C. Li, S. Zheng, Construction of  $\text{BiOCl}/\text{g-C}_3\text{N}_4/\text{kaolinite}$  composite and its enhanced photocatalysis performance under visible-light irradiation, *J. Taiwan Inst. Chem. Eng.* 84 (2018) 203–211.
- T. Zhang, H. Zhu, J.P. Croué, Production of sulfate radical from peroxymonosulfate induced by a magnetically separable  $\text{CuFe}_2\text{O}_4$  spinel in water: efficiency, stability, and mechanism, *Environ. Sci. Technol.* 47 (2013) 2784–2791.
- Y. Feng, D. Wu, Y. Deng, T. Zhang, K. Shih, Sulfate radical-mediated degradation of sulfadiazine by  $\text{CuFe}_2\text{O}_4$  rhombohedral crystal-catalyzed peroxymonosulfate: synergistic effects and mechanisms, *Environ. Sci. Technol.* 50 (2016) 3119–3127.
- P. Shukla, S. Wang, H. Sun, H. Ang, M. Tade, Activated carbon supported cobalt catalysts for advanced oxidation of organic contaminants in aqueous solution, *Appl. Catal. B: Environ.* 100 (2010) 529–534.
- Y. Xie, P. Li, Y. Zeng, X. Li, Y. Xiao, Y. Wang, Y. Zhang, Thermally treated fungal manganese oxides for bisphenol A degradation using sulfate radicals, *Chem. Eng. J.* 335 (2018) 728–736.
- A.H. Mady, M.L. Baynosa, D. Tuma, J.J. Shim, Heterogeneous activation of peroxymonosulfate by a novel magnetic 3D  $\gamma\text{-MnO}_2/\text{ZnFe}_2\text{O}_4/\text{rGO}$  nanohybrid as a robust catalyst for phenol degradation, *Appl. Catal. B: Environ.* 244 (2019) 946–956.
- H. Sun, C. Kwan, A. Suvorova, H. Ang, M. Tade, S. Wang, Catalytic oxidation of organic pollutants on pristine and surface nitrogen-modified carbon nanotubes with sulfate radicals, *Appl. Catal. B: Environ.* 154–155 (2014) 134–141.
- X. Li, Z. Ao, J. Liu, H. Sun, A.I. Rykov, J. Wang, Topotactic transformation of metal-organic frameworks to graphene-encapsulated transition-metal nitrides as efficient Fenton-like catalysts, *ACS Nano* 10 (2016) 11532–11540.
- M. Marjanovic, S. Giannakis, D. Grandjean, L.A. De, C. Pulgarin, Effect of  $\mu\text{M}$  Fe addition, mild heat and solar UV on sulfate radical-mediated inactivation of bacteria, viruses, and micropollutant degradation in water, *Water Res.* 140 (2018) 220–231.
- X. He, A.A.D.L. Cruz, D.D. Dionysiou, Destruction of cyanobacterial toxin cylindrospermopsin by hydroxyl radicals and sulfate radicals using UV-254 nm activation of hydrogen peroxide, persulfate and peroxymonosulfate, *J. Photochem. Photobiol. A: Chem.* 251 (2013) 160–166.
- C. Jiang, Y. Ji, Y. Shi, J. Chen, T. Cai, Sulfate radical-based oxidation of fluor-quinolone antibiotics: kinetics, mechanisms and effects of natural water matrices, *Water Res.* 106 (2016) 507–517.
- Z. Liu, C. Zhao, P. Wang, H. Zheng, Y. Sun, D.D. Dionysiou, Removal of carbamazepine in water by electro-activated carbon fiber-peroxydisulfate: comparison, optimization, recycle, and mechanism study, *Chem. Eng. J.* 343 (2018) 28–36.
- K. Faungnawakij, N. Viriya-empikul, Catalytic behavior toward oxidative steam reforming of dimethyl ether over  $\text{CuFe}_2\text{O}_4\text{-Al}_2\text{O}_3$  composite catalysts, *Appl. Catal. A: Gen.* 382 (2010) 21–27.
- Y. Wang, H. Zhao, M. Li, J. Fan, G. Zhao, Magnetic ordered mesoporous copper ferrite as a heterogeneous Fenton catalyst for the degradation of imidacloprid, *Appl. Catal. B: Environ.* 147 (2014) 534–545.
- Y. Yao, Y. Cai, F. Lu, F. Wei, X. Wang, S. Wang, Magnetic recoverable  $\text{MnFe}_2\text{O}_4$  and  $\text{MnFe}_2\text{O}_4$ -graphene hybrid as heterogeneous catalysts of peroxymonosulfate activation for efficient degradation of aqueous organic pollutants, *J. Hazard. Mater.* 270 (2014) 61–70.
- T. Xu, G. He, Y. Zhao, H. Gu, Z. Jiang, Q. Chen, X. Sun, H. Chen, Benzenoid-like  $\text{CuFe}_2\text{O}_4$ /reduced graphene oxide: facile synthesis and its excellent catalytic performance in selective oxidation, *Appl. Surf. Sci.* 389 (2016) 840–848.
- X. Zhang, M. Feng, R. Qu, H. Liu, L. Wang, Z. Wang, Catalytic degradation of diethyl phthalate in aqueous solution by persulfate activated with nano-scaled magnetic  $\text{CuFe}_2\text{O}_4/\text{MWCNTs}$ , *Chem. Eng. J.* 301 (2016) 1–11.
- C. Li, Z. Sun, A. Song, X. Dong, S. Zheng, D.D. Dionysiou, Flowing nitrogen atmosphere induced rich oxygen vacancies overspread the surface of  $\text{TiO}_2/\text{kaolinite}$  composite for enhanced photocatalytic activity within broad radiation spectrum, *Appl. Catal. B: Environ.* 236 (2018) 76–87.
- C. Li, Z. Sun, W. Zhang, C. Yu, S. Zheng, Highly efficient  $\text{g-C}_3\text{N}_4/\text{TiO}_2/\text{kaolinite}$  composite with novel three-dimensional structure and enhanced visible light responding ability towards ciprofloxacin and *S. aureus*, *Appl. Catal. B: Environ.* 220 (2018) 272–282.
- P. Srivastava, B. Singh, M. Angove, Competitive adsorption behavior of heavy metals on kaolinite, *J. Colloid Interface Sci.* 290 (2005) 28–38.
- C. Li, Y. Huang, X. Dong, Z. Sun, X. Duan, B. Ren, S. Zheng, D.D. Dionysiou, Highly efficient activation of peroxymonosulfate by natural negatively-charged kaolinite with abundant hydroxyl groups for the degradation of atrazine, *Appl. Catal. B: Environ.* 247 (2019) 10–23.
- Y. Ding, L. Zhu, N. Wang, H. Tang, Sulfate radicals induced degradation of tetrabromobisphenol A with nanoscaled magnetic  $\text{CuFe}_2\text{O}_4$  as a heterogeneous catalyst of peroxymonosulfate, *Appl. Catal. B: Environ.* 129 (2013) 153–162.
- M.S. Zbik, N.A. Raftery, R.S.C. Smart, R.L. Frost, Kaolinite platelet orientation for XRD and AFM applications, *Appl. Clay Sci.* 50 (2010) 299–304.
- A.D. Al-Rawas, H.M. Widatallah, I.A. Al-Omari, C. Johnson, M.E. Elzain, A.M. Gismelseed, S. Al-Taie, A.A. Yousif, The Influence of mechanical milling and subsequent calcination on the formation of nanocrystalline  $\text{CuFe}_2\text{O}_4$ , *AIP Conf. Proc.* 765 (2005) 277–281.
- C. Karthikeyan, K. Ramachandran, S. Sheet, J.Y. Dong, S.L. Yang, Y.S. Kumar, A.R. Kim, G.G. Kumar, Pigeon-excreta-mediated synthesis of reduced graphene oxide ( $\text{rGO}$ )/ $\text{CuFe}_2\text{O}_4$  nanocomposite and its catalytic activity toward sensitive and selective hydrogen peroxide detection, *ACS Sustain. Chem. Eng.* 5 (2017) 4879–4905.
- Y. Deng, J. Wei, Z. Sun, D. Zhao, Large-pore ordered mesoporous materials templated from non-pluronic amphiphilic block copolymers, *Chem. Soc. Rev.* 42 (2013) 4054–4070.
- A. Vinu, V. Murugesan, O. Tagermann, M. Hartmann, Adsorption of cytochrome c on mesoporous molecular sieves: influence of pH, pore diameter, and aluminum incorporation, *Chem. Mater.* 16 (2004) 3056–3065.
- L. Deng, Y. Xie, G. Zhang, Synthesis of C-Cl-codoped titania/attapulgite composites with enhanced visible-light photocatalytic activity, *Chin. J. Catal.* 38 (2017) 379–388.
- J. Yao, X. Zeng, Z. Wang, Enhanced degradation performance of sulfisoxazole using peroxymonosulfate activated by copper-cobalt oxides in aqueous solution: kinetic study and products identification, *Chem. Eng. J.* 330 (2017) 345–354.
- X. Li, X. Huang, S. Xi, S. Miao, J. Ding, W. Cai, S. Liu, X. Yang, H. Yang, J. Gao,

- J. Wang, Y. Huang, T. Zhang, B. Liu, Single cobalt atoms anchored on porous N-doped graphene with dual reaction sites for efficient Fenton-like catalysis, *J. Am. Chem. Soc.* 140 (2018) 12469–12475.
- [41] P. Neta, R.E. Huie, A.B. Ross, Rate constants for reactions of inorganic radicals in aqueous solution, *J. Phys. Chem. Ref. Data* 17 (1988) 1027–1284.
- [42] H. Zhao, J. Joseph, H.M. Fales, E.A. Sokoloski, R.L. Levine, J. Vasquez-Vivar, B. Kalyanaraman, Detection and characterization of the product of hydroethidine and intracellular superoxide by HPLC and limitations of fluorescence, *Proc. Natl. Acad. Sci. U. S. A.* 102 (2005) 5727–5732.
- [43] G. Fang, J. Gao, D.D. Dionysiou, C. Liu, D. Zhou, Activation of persulfate by quinones: free radical reactions and implication for the degradation of PCBs, *Environ. Sci. Technol.* 47 (2013) 4605–4611.
- [44] Z. Xu, C. Shan, B. Xie, Y. Liu, B. Pan, Decomplexation of Cu(II)-EDTA by UV/persulfate and UV/H<sub>2</sub>O<sub>2</sub>: efficiency and mechanism, *Appl. Catal. B: Environ.* 200 (2017) 439–447.
- [45] C. Liang, H.W. Su, Identification of sulfate and hydroxyl radicals in thermally activated persulfate, *Ind. Eng. Chem. Res.* 48 (2009) 472–475.
- [46] T. Zhang, C. Li, J. Ma, H. Tian, Z. Qiang, Surface hydroxyl groups of synthetic  $\alpha$ -FeOOH in promoting OH generation from aqueous ozone: property and activity relationship, *Appl. Catal. B: Environ.* 82 (2008) 131–137.
- [47] J. Gonzalez, M. Torrent-Sucarrat, J.M. Anglada, The reactions of SO<sub>3</sub> with HO<sub>2</sub> radical and H<sub>2</sub>O...HO<sub>2</sub> radical complex. Theoretical study on the atmospheric formation of HSO<sub>5</sub> and H<sub>2</sub>SO<sub>4</sub>, *Phys. Chem. Chem. Phys.* 12 (2010) 2116–2125.
- [48] Y. Lei, C.S. Chen, Y.J. Tu, Y.H. Huang, H. Zhang, Heterogeneous degradation of organic pollutants by persulfate activated by CuO-Fe<sub>3</sub>O<sub>4</sub>: mechanism, stability, effects of pH and bicarbonate ions, *Environ. Sci. Technol.* 49 (2015) 6838–6845.
- [49] Y. Ding, H. Tang, S. Zhang, S. Wang, H. Tang, Efficient degradation of carbamazepine by easily recyclable microscaled CuFeO<sub>2</sub> mediated heterogeneous activation of peroxymonosulfate, *J. Hazard. Mater.* 317 (2016) 686–694.
- [50] Y. Xu, J. Ai, H. Zhang, The mechanism of degradation of bisphenol A using the magnetically separable CuFe<sub>2</sub>O<sub>4</sub>/peroxymonosulfate heterogeneous oxidation process, *J. Hazard. Mater.* 309 (2016) 87–96.
- [51] Y. Huang, C. Han, Y. Liu, M.N. Nadagouda, L. Machala, K.E. O'Shea, V.K. Sharma, D.D. Dionysiou, Degradation of atrazine by Zn<sub>x</sub>Cu<sub>1-x</sub>Fe<sub>2</sub>O<sub>4</sub> nanomaterial -catalyzed sulfite under UV-vis light irradiation: green strategy to generate SO<sub>4</sub><sup>-</sup>, *Appl. Catal. B: Environ.* 221 (2018) 380–392.
- [52] C. Wei, J. Zhang, Y. Zhang, G. Zhang, P. Zhou, W. Li, J. Liang, Y. Liu, W. Zhang, Ultrasound enhanced heterogeneous activation of peroxymonosulfate by a Co-NiO<sub>x</sub> catalyst, *Water Sci. Technol.* 76 (2017) 1436–1446.
- [53] L. Chen, X. Zuo, L. Zhou, Y. Huang, S. Yang, T. Cai, D. Ding, Efficient heterogeneous activation of peroxymonosulfate by facilely prepared Co/Fe bimetallic oxides: kinetics and mechanism, *Chem. Eng. J.* 345 (2018) 364–374.
- [54] P. Hu, M. Long, Cobalt-catalyzed sulfate radical-based advanced oxidation: a review on heterogeneous catalysts and applications, *Appl. Catal. B: Environ.* 181 (2016) 103–117.
- [55] X. Lou, L. Wu, Y. Guo, C. Chen, Z. Wang, D. Xiao, C. Fang, J. Liu, J. Zhao, S. Lu, Peroxymonosulfate activation by phosphate anion for organics degradation in water, *Chemosphere* 117 (2014) 582–585.
- [56] Z. Yang, D. Dai, Y. Yao, L. Chen, Q. Liu, L. Luo, Extremely enhanced generation of reactive oxygen species for oxidation of pollutants from peroxymonosulfate induced by a supported copper oxide catalyst, *Chem. Eng. J.* 322 (2017) 546–555.
- [57] J. Huang, X. Li, M. Ma, D. Li, Removal of di-(2-ethylhexyl) phthalate from aqueous solution by UV/peroxymonosulfate: influencing factors and reaction pathways, *Chem. Eng. J.* 314 (2017) 182–191.
- [58] Y. Wang, D. Cao, X. Zhao, Heterogeneous degradation of refractory pollutants by peroxymonosulfate activated by CoO<sub>x</sub>-doped ordered mesoporous carbon, *Chem. Eng. J.* 328 (2017) 1112–1121.
- [59] R. Yuan, S.N. Ramjaun, Z. Wang, J. Liu, Effects of chloride ion on degradation of Acid Orange 7 by sulfate radical-based advanced oxidation process: implications for formation of chlorinated aromatic compounds, *J. Hazard. Mater.* 196 (2011) 173–179.
- [60] S. Luo, J. Xu, Z. Li, C. Liu, J. Chen, X. Min, M. Fang, Z. Huang, Bismuth oxyiodide coupled with bismuth nanodots for enhanced photocatalytic bisphenol A degradation: synergistic effects and mechanistic insight, *Nanoscale* 42 (2017) 15484–15493.
- [61] L. Xu, L. Yang, E.M.J. Johansson, Y. Wang, P. Jin, Photocatalytic activity and mechanism of bisphenol A removal over TiO<sub>2-x</sub>/rGO nanocomposite driven by visible light, *Chem. Eng. J.* 350 (2018) 1043–1055.
- [62] Y. Zhang, N. Qin, J. Li, S. Han, P. Li, G. Zhao, Facet exposure-dependent photoelectrocatalytic oxidation kinetics of bisphenol A on nanocrystalline {001} TiO<sub>2</sub>/carbon aerogel electrode, *Appl. Catal. B: Environ.* 216 (2017) 30–40.